Comparison of pilot fuel ignited premixed ammonia versus methane dual-fuel combustion

S. Wüthrich, P. Albrecht, P. Cartier, and K. Herrmann
Institute of Thermal and Fluid Engineering (ITFE),
University of Applied Sciences and Arts Northwestern Switzerland (FHNW)
Klosterzelgstrasse 2, CH-CH-5210 Windisch, Switzerland

Conference Proceedings - Rostock Large Engine Symposium 2022

Prof. Dr.-Ing. Bert Buchholz (Editor)

and 75 co-authors

ISBN 978-3-941554-25-2

The future of large engines VII

7th Large Engine Symposium, Rostock 2022

The Future of Large Engines

Technology Concepts and Fuel Options – Pathways to Clean Shipping

with 237 figures und 37 tables

FVTR textbook series

The future of large engines VII

1st edition

Rostock, September 2022
FVTR textbook series

Published by

Joachim-Jungius-Str. 9, D-18059 Rostock, Germany

Tel.: +49 381-4059650

Fax: +49 381-4059657

E-mail: office@fvtr.de

Web: https://fvtr.de/

Comparison of pilot fuel ignited premixed ammonia versus methane dual-fuel combustion

Silas Wüthrich, Patrick Albrecht, Patrick Cartier, and Kai Herrmann

Institute of Thermal and Fluid Engineering (ITFE)
University of Applied Sciences and Arts Northwestern Switzerland (FHNW)
Klosterzelgstrasse 2, CH-5210 Windisch, Switzerland

Abstract

In view of reducing greenhouse gas emissions the transition from fossil fuels to sustainable energy carriers is a prerequisite to keep global warming within tolerable limits. Since IC engines will continue to play a role in global energy strategies during a transitional phase, especially for large engine applications difficult to electrify, the use of ammonia as substitute fuel may be an approach for decarbonization. However, its utilization needs research since ignition concepts and combustion properties still pose considerable challenges in view of reliable and efficient operation.

The optical engine test facility *Flex-OeCoS* has been successfully adapted enabling dodecane pilot fuel ignited premixed ammonia dual-fuel combustion investigations. It features IC engine relevant operation conditions such as pressures, temperatures, and flow (turbulence) conditions as well as adjustable mixture charge composition and pilot fuel injection settings. Thermodynamic heat release analysis in terms of ignition and combustion characteristics has been established. Simultaneously applied high-speed Schlieren/OH* chemiluminescence measurements allow the examination of the combustion process.

Premixed ammonia dual-fuel combustion has been compared to methane combustion process. Ignition delay, combustion transition, and turbulent flame propagation as well as heat release characteristics have been investigated within variation of air-fuel equivalence ratio, start of pilot fuel injection, and other operation conditions. Different gas properties (lower heating value, air-fuel ratio) illustrate ammonia lower reactivity affecting heat release and flame propagation. Moreover, strong dependency on air-fuel equivalence ratio (energy content) and temperature conditions in terms of ignition delay, dual-fuel combustion transition, and corresponding heat release is present. The optical investigations confirm the thermodynamic analysis and promote assessment of pilot fuel evaporation, ignition, combustion transition, and flame propagation. Conclusions give insight into the thermo-chemical processes of ammonia pilot fuel ignited dual-fuel combustion.

1. Introduction

The aim towards a carbon-neutral society is set out in the Paris Agreement, a legally binding international treaty on climate change, and aims to keep the rise in global average temperature to well below 2°C above pre-industrial levels and to step up efforts to limit the temperature increase to 1.5°C [1]. Thus, it is a requirement over the course of this century that private as well as industrial sectors reduce their greenhouse gas emissions to zero. In addition to a continuous improvement of energy efficiency through technical and operational measures, electrification based on renewable energies is the most efficient approach to achieve this goal. On the other hand, due to the limited energy density of batteries, direct use of electricity is limited or not possible in certain applications within industrial sectors. This is particularly true for the marine sector, where – apart from certain niche applications, such as ferries or short sea shipping – the switch from fossil to renewable fuels is one of the most promising options for decarbonization. Since large IC engines will continue to play a role for marine propulsion, the transition from fossil fuels to sustainable energy carriers is one of the necessities in view of reducing greenhouse gas emissions to keep global warming within tolerable limits. Sustainable fuels can be generated either through synthesis based on renewable energy or from the processing of biological wastes and residues. The potential of biofuels is limited in terms of quantity, where synthetic fuels are associated with a price penalty depending on the refinement level.

Various technology paths for internal combustion engines and fuel systems for future propulsion of ships have been investigated. For the substitution of fossil fuels, ammonia or methanol were identified as potential candidates for an economically feasible route to decarbonization [2]. Of course, these fuels must be produced via renewable energy and only ammonia can be considered CO_2-free – since methanol still contains carbon, the CO_2 needed for production must come from non-fossil sources (direct air capture) to at least be considered carbon neutral. All possible options with respect to use as a post-fossil fuel – including "green" hydrogen for certain applications – have advantages and disadvantages in terms of scope, handling, efficiency, cost, environmental risks, etc. In particular, the use of ammonia has recently gained increasing attention and is being touted by various stakeholders as one of the most promising future fuels. Various studies have investigated the potential for application in marine shipping from a cost and production point of view [3-8]. Although ammonia is a well-known product since centuries, it has mainly been used to produce fertilizers and has not yet been used on a larger scale as a fuel. In terms of future engine and fuel systems, various transition phases are expected up to 2050. In the current decade, the share of liquefied natural gas (LNG) will probably still increase before the desired transition to methanol or ammonia takes place. Even if the use of sustainable fuels produced by the synthesis of renewable energies (Power-to-X or synfuels) or from the processing of suitable biological wastes and residues (biofuels) is mandatory, the use of LNG as a marine fuel will probably still be a given in a transition phase in the next decade and beyond.

Current concepts of gas engines are seen as good basis for future solutions designed for operation on such alternative fuels. Even though ammonia fuel application for IC engines is not new, the conversion still providing comparable efficiency and guaranteeing reliable operation, poses certain challenges in terms of ignition concepts and combustion properties. A range of involved complex processes such as flow field conditions, evaporation and mixing properties, ignition, combustion onset, and flame propagation need to be considered. In this work, an optically accessible experimental test facility providing engine relevant operation conditions was used to fundamentally examine premixed pilot fuel ignited

methane vs. ammonia dual-fuel (DF) combustion. The investigations include levels of typical operating conditions for marine dual-fuel engines with compression temperatures around 800 K and peak pressures up to 180 bar and beyond. The influence of different operation parameters, such as mixture charge composition or process temperatures and pressures has been investigated. First insight into the thermo-chemical processes of combustion in terms of ignition delay, combustion onset, dual-fuel combustion transition, turbulent flame propagation, and heat release shall be provided.

2. Experimental setup, test execution and analysis

The optically accessible test facility *Flex-OeCoS* enables examination of premixed pilot fuel ignited dual-fuel combustion processes in a range of IC engine relevant operational parameters [9]. Acquisition of crank-angle resolved operating conditions in terms of precise pressure as well as temperature measurements (by fine-wire thermocouples at different locations), and turbulent flow field determination (by means of high-speed PIV) has been established [10]. The adaptable setup with flexible operation modes has already been used for different dual-fuel combustion process investigations [11-14].

2.1. Test facility Flex-OeCoS

Figure 1 shows the working principle of the *Flex-OeCoS* test rig: One cylinder of a motor driven engine block feeds a mixture charge into an optical combustion chamber (Ø60 mm×20 mm), providing maximum optical access through rectangular and round sapphire windows at each side. Two intake valves (Ø16 mm) are located on the working cylinder, which is equipped with a flat-top piston. Two exhaust valves (Ø16 mm) are positioned on top of the combustion chamber, where a central bore at the top allows mounting of a pilot fuel injector, spark plug or pre-chamber. Various pressure sensors are implemented at different locations, and the entire head is thermally conditioned to achieve stable conditions during the aperiodic operation.

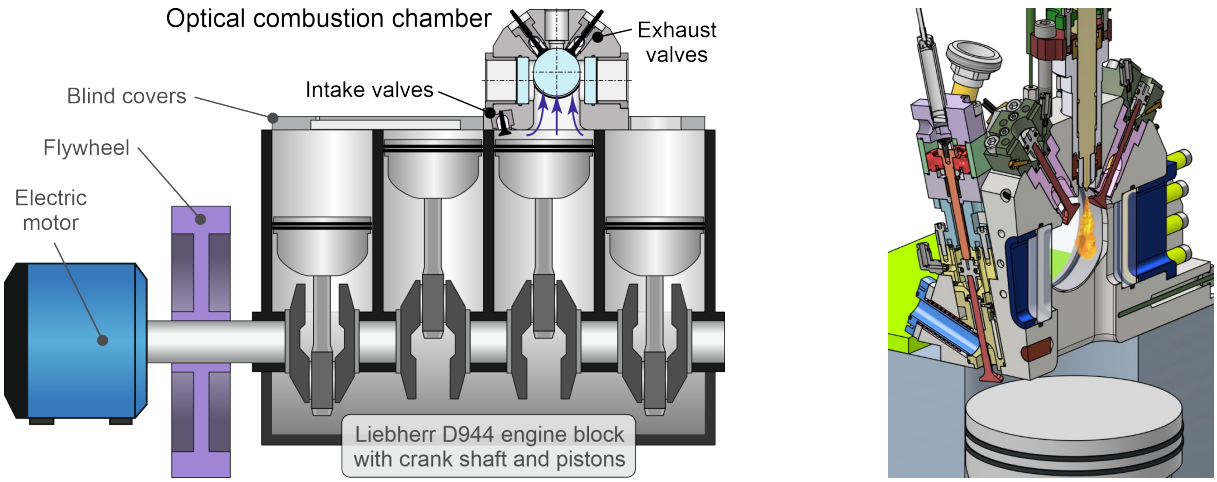

Figure 1: Concept of the Flex-OeCoS test facility. (left) and cylinder head on the working cylinder with optical combustion chamber, intake/exhaust valves, and centered pilot fuel injector (right).

The *Flex-OeCoS* test facility features adaptable operation at IC engine relevant conditions: peak pressures of up to 240 bar (from boost-adjustable compression pressure p_c up to 130 bar), mixture charge temperatures T between 700 – 1000 K by inlet conditioning, and tunable flow (turbulence grades) depending on motor speed n of typically 300 – 1000 rpm. An overview of relevant test facility specifications is given in Table 1.

Table 1: Test facility specifications and parameter settings.

Dimensions, Operating Parameter		
Working cylinder bore	Ø 130	[mm]
Stroke length	150	[mm]
Connecting rod length	237.1	[mm]
Displacement (working cylinder)	1990	[cm^3]
Compression ratio	13.8	[-]
Optical combustion chamber diameter/height	Ø 60 / 20	[mm]
Max. cylinder pressure	240	[bar]
Motor speed range	300 - 1000	[rpm]

Reference values (air charge)		
Intake boost pressure p_b	2.65 / 4.4 / 5.8	[bar]
Compression pressure p_c	70 / 100 / 130	[bar]
Intake temperature T_{in}	50 / 100	[°C]
Motor speed n	600	[rpm]
Turbulence intensity u' [9]	3.6	[m/s]

Independent pneumatic intake and exhaust valve actuators provide high variability. Moreover, pilot fuel injection settings (pressure, start, and duration) as well as mixture charge composition, by gas introduction in the air inlet pipe close to the intake valve, can be freely set by external supply units.

2.2. Optical setup, methodology and post-processing

As illustrated in Figure 2 simultaneous high-speed Schlieren/OH* chemiluminescence was applied to investigate pilot fuel injection and evaporation, dual-fuel ignition processes, turbulent flame front propagation, and combustion characteristics. Image acquisition was performed by means of two high-speed cameras: The chemiluminescence of the OH* radical as indicator of inflammation was acquired simultaneously with the Schlieren signal indicating liquid and vaporized phases. The spatial resolution has been set to 60×60 mm (covering the entire combustion chamber) to achieve a temporal resolution of 0.1 °CA, for the typical motor speed of n = 600 rpm, resulting in a frame rate of 36 kHz.

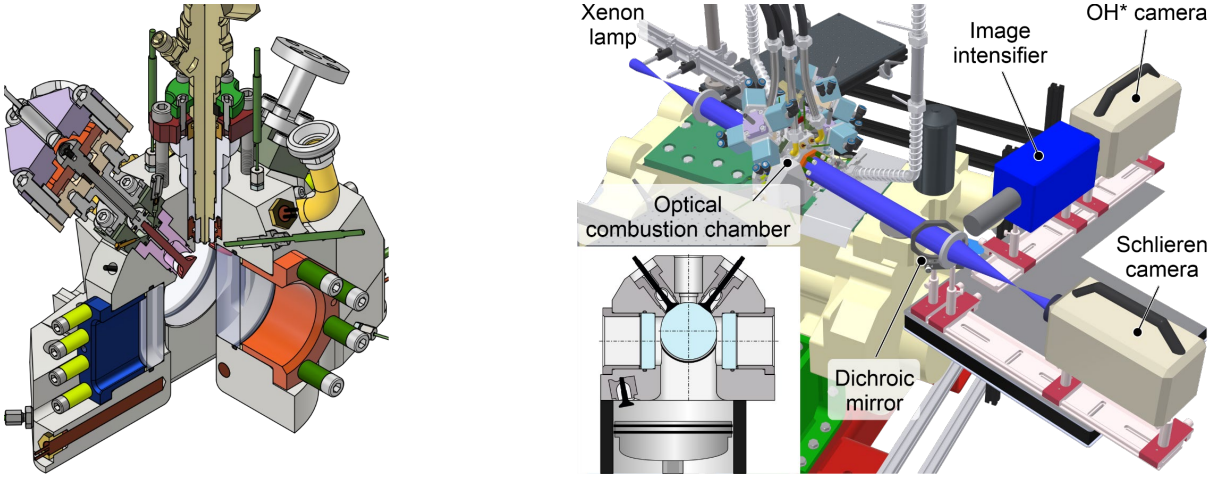

Figure 2: Optically accessible combustion chamber (left) and setup of simultaneously applied Schlieren and OH chemiluminescence measurement techniques (right).*

The determination of the effective start of injection *SOI* is based on the Schlieren spray contour. Due to high turbulence levels, a detection of the spray/flame with a threshold value often leads to errors. Thus, detection is based on a predefined probability density function dependent on the image zone (background, dense core, flame) to assign pixel values to a specific location. However, even highest camera frame rates never facilitate a systematic capture of every actual injection begin, since it cannot be accurately timed due to the inherent slightly deviating hydraulic delay of the injector. According to the realistic assumption that the spray area increases linearly at first, the effective start of injection was extrapolated from evaluated spray area values.

The OH* chemiluminescence corresponds to ignition and represents an integrated line-of-sight signal along the entire measurement volume. Even though other species (e.g. CO*), particularly under lean conditions at high pressures, may contribute considerably to the overall OH* signal at progressing combustion [15], the first OH* chemiluminescence emission appears at least simultaneously at ignition [16]. Moreover, also the interference of soot incandescence does not (yet) affect the ignition detection [17]. The start of (high temperature) combustion therefore has been defined as the first OH* appearance, respectively the first image containing a "brighter spot" [18]. The automated optical ignition delay detection proved to be reliable, also compared to the corresponding ignition delay detection from the heat release analysis.

2.3. Measurement procedure and analysis

The settings in Table 1 (intake temperature T_{in}, boost/compression pressures p_b/p_c, turbulence intensity u') are based on pure air compression. These are denoted as reference values for all gas/air pilot fuel ignited dual-fuel investigations, where certain parameters, such as effective compression pressure p_c and temperature T_c, are dependent on the specific gas respectively mixture charge properties.

Table 2 gives an overview of performed measurements operation settings in terms of ammonia/air or methane/air mixture charge conditions such as air-fuel equivalence ratio λ and start of pilot fuel injection (*SOI*). It additionally includes the variation of settings for the dodecane pilot fuel injection (Bosch CRI-2 solenoid injector) through a Ø103 µm single-hole nozzle. Injection pressure, start and duration (based on initially determined injection rate characteristics according to energizing time) can be set independently by a separate fuel supply unit. However, the results presented here refer to a constant injection duration (*DOI*) only, to allow an evaluation of other operating parameters unaffected by this.

Table 2: Measurement operation and pilot fuel injection parameter settings.

NH_3/air and CH_4/air mixture charge		
Air-fuel equivalence ratio λ_{NH3}	2.0 / 1.75 / 1.5 / 1.25 / 1.0	
Air-fuel equivalence ratio λ_{CH4}	0.8 – 3.0 (in 0.1 steps)	
Start of gas admission	60 °CA before intake valve opens	[°CA]
Compression pressure p_c	*setting dependent* → see results	[bar]
Compression temperature T_c	*setting dependent* → see results	[K]

Pilot fuel injection parameters		
Pilot fuel	Dodecane	
Nozzle diameter d_{nozzle}	Ø 103 (measured)	[µm]
Injection pressure p_{inj}	1000	[bar]
Start of injection *SOI*	−20 / −15 / −10 / −5 / 0	[°CA]
Energizing time *ET*	500	[µs]
Duration of injection *DOI*	523	[µs]

Start of injection, ignition delay (location), combustion onset, and flame propagation have been evaluated by post-processing procedures of the simultaneously applied Schlieren and OH* chemiluminescence measurements. Combustion heat release rate has been analyzed applying an in-house thermodynamic 2-zone model considering dissociation in the burnt gas zone, accounting for losses by wall heat transfer, piston ring blow-by, and crevice volumes [19]. Due to the unique test facility layout (optical combustion chamber vs. working cylinder), significant efforts were made in terms of high precision pressure acquisition [20]. The wall heat losses were estimated using an adapted *Woschni* approach (inclusive extended heat transfer coefficient α_W based on flow measurements), piston-ring blow-by was measured, and the volume of crevices were determined by drawings. However, since the wall-heat loss model had to be tuned by distinctive constants the results are denoted as apparent heat release rate *aHRR*.

Ignition delay can be deduced from both optical data (OH* chemiluminescence) and from the calculated heat release rates. The total energy available for combustion is the sum of the energy content in the injected pilot fuel and the energy contained in the premixed cylinder charge. By assuming that the pilot spray energy content has been unleashed completely before the main charge starts to burn it is possible to define a threshold level of the heat release that marks the onset of the premixed mixture combustion. This delay between ignition and the moment when the heat release is exceeding the energy content of the injected pilot fuel is denoted as *transition time*. The energy from the premixed charge entrained in the evaporating fuel spray and combusting together with it is not considered in this definition. Therefore, the longer the ignition delay, the larger the amount of premixed charge combusting together with the pilot fuel, and the more this transition time underestimates the time required to burn the complete evaporated fuel spray volume. Nonetheless this time is an important value to characterize DF combustion and reflects the reactivity at the temperature/pressure conditions during inflammation.

An *apparent flame propagation speed* s_{aFP} can be determined by the Schlieren measurements, respectively the contour displacement representing the flame surface. The method applied here consists of a two-dimensional spatially averaged evaluation of reaction zone expansion based on the optical measurements. It resolves local behaviour very well (i.e. large propagation speeds) but is also more prone to misidentification of burned zones since still containing certain uncertainty in differentiation of refractive index variation. In addition, the effect of flame compression and expansion cannot be corrected for distinctive pressure variations, and the determined s_{aFP} always includes the effect of the expanding burned zone. Thus, higher pressure ratios are affecting the resulting s_{aFP} stronger for lower air-fuel equivalence ratios. However, the chosen approach can deal with (local) transport phenomena and leads to an accurate statement in terms of the early combustion phase. The designation "apparent" shall point out that the analyzed flame propagation speed must be interpreted as a qualitative value nevertheless enabling a comparison within operation parameter variation.

The properties of the compared fuels (ammonia vs. methane), and dodecane as pilot fuel are shown in Table 3. The low flame speed of ammonia results in a slower combustion process which can reduce the combustion efficiency. The high auto-ignition temperature and enormous heat of vaporization makes liquid injection and diesel-like compression ignition combustion difficult. The high minimum ignition energy means that it is comparably more difficult to safely ignite an ammonia-air mixture. The high resistance to knocking (*RON*) allows to run ammonia fueled engines at higher compression ratios, which can be beneficial for efficiency. Although ammonia has a much lower energy content per mass than carbon-based standard fuels, its low stoichiometric air-fuel ratio *AFR* partly compensates this regarding the in-cylinder energy content.

Table 3: Properties of ammonia, methane, and the pilot fuel n-dodecane. Data collected for comparison only from [21-26].

	Storage conditions	Density @ storage conditions [kg/m³]	LHV @ storage conditions	Flammability limits in air [Vol-%]	Stoichiometric AFR (mass) [-]	LHV per Vol. @ stoichiometry (0.1 MPa, 373 K) [MJ/m³]	Auto-ignition temperature [K]	Minimum ignition energy [mJ]	Heat of vaporization [kJ/kg]	LBV @ stoichiometry (0.1 MPa, 300 K) [m/s]	RON [-]
Ammonia NH_3 (Liquid)	1.1 MPa 300 K	600	18.8 MJ/kg 11.3 GJ/m³	15 – 28	6.1 : 1	~ 2.23	930	8	1370	0.07	> 130
Methane CH_4 (Compressed)	25 MPa 300 K	187	50 MJ/kg 9.4 GJ/m³	5 – 15	17.3 : 1	~ 2.45	860	~ 0.21	–	0.38	120
n-Dodecane $C_{12}H_{26}$ (Diesel)	0.1 MPa 300 K	750	45 MJ/kg 33 GJ/m³	0.6 – 7.5	~ 15 : 1	–	480	(Diesel ~0.23)	256	~ 0.8	–

3. Results

The presented results yield partly from further data analysis of an initial ammonia measurement campaign [14] and correspondingly performed additional measurements for the methane case. An insight into ammonia vs. methane dual-fuel combustion initiated by a dodecane pilot in terms of ignition delay, combustion onset, dual-fuel combustion transition, flame propagation, and heat release is given.

3.1. Variation of air-fuel equivalence ratio λ

Figure 3 shows a comparison of the pressure development for methane vs. ammonia charge mixtures with air-fuel equivalence ratio λ = 1.0 / 1.5 / 2.0. The dodecane pilot fuel injection (*ET* = 500 µs) was initiated at *SOI* = -10 °CA, corresponding to a compression temperature of about 790 K, for both cases [14]. The pressure trace represents the averaged value of twenty-five combustion cycles superimposed by the standard deviation (*STD*). In terms of energy respectively heat release, two aspects must be considered: On the one hand, the specific heating value of ammonia is less than half compared to methane (Table 3, *LHV*: 18.8 MJ/kg vs. 50 MJ/kg). On the other hand, for stoichiometric combustion ammonia needs less air (Table 3, *AFR*: 6.1 vs. 17.3) than methane. Ultimately, the (constant) mixture charge volume in the *Flex-OeCoS* test facility during an experimental cycle leads to slightly different energy content of ammonia vs. methane combustion. Thus, for an air-equivalence ratio of λ = 1.0, the energy content of the ammonia/air mixture is 7.7 % lower than the one for the methane case. Correspondingly, for λ = 1.5 and λ = 2.0 the energy content is 3.7 % and 1.5 % lower, respectively.

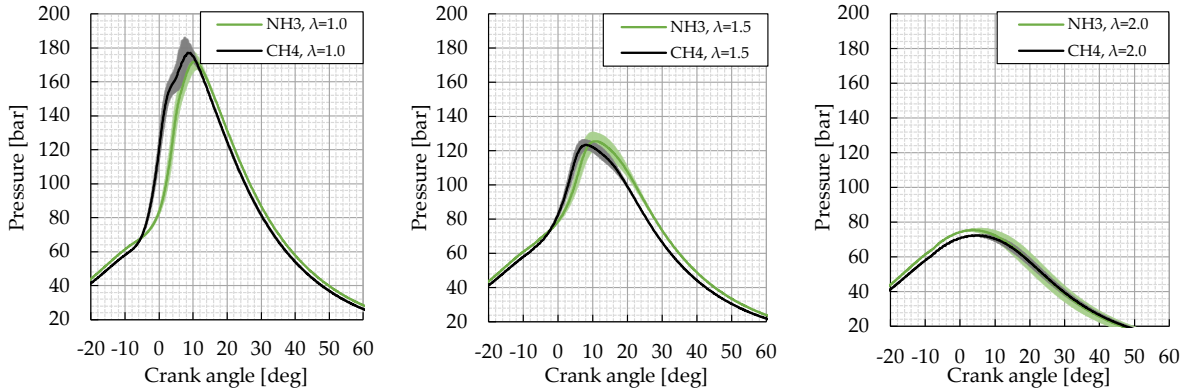

Figure 3: Cylinder pressure of pilot fuel ignited ammonia vs. methane DF combustion (incl. standard deviation) for λ = 1.0 / 1.5 / 2.0 at operation parameters p_c = 70 bar, T_{in} = 50 °C, SOI = −10 °CA, ET = 500 µs.

Assuming identical combustion conversion rates, peak pressures only depend on energy amount and position of the center of combustion. Regarding *LHV* respectively *AFR*, the pressure rise due to combustion is, especially at low air-fuel equivalence ratios, for ammonia slightly lower than for methane, as expected. The lower pressure rise rate of ammonia, due to its lower reactivity, shifts the center of combustion to a later position. Nevertheless, the achieved cylinder pressure is quite surprising regarding the low laminar flame speed which implicates a much slower burn rate compared to methane.

In Figure 4 the apparent heat release rates *aHRR* are shown. Again, due to the higher reactivity of the air/methane/dodecane mixture, heat release rates rise much faster compared to ammonia, but the *aHRR* peak levels and its maximum gradients are quite similar. The standard deviation (indicated in pale color) is even slightly smaller for ammonia combustion compared to methane. This can be explained by the fact that the lower reactivity of ammonia means that less fuel is ignited at a high burn rate, which causes combustion chamber oscillations. These are easily recognizable in the *aHRR* and occur especially

when the combustion zone reaches the squish gap. Additionally, a distinct two-phase heat release can be observed for methane (less pronounced for ammonia), which is related to the special design of the test rig: The tilted optical combustion chamber is fed by the working cylinder, where those two connected volumes cause a staged combustion process. The flame expanding through the optical combustion chamber can further propagate through the narrow connection into the engine cylinder to burn the charge in the design related large squish gap area. This effect is more pronounced for faster heat releases since for slower processes combustion in the optical chamber and the working cylinder overlap, which renders the staged combustion process less obvious. Thus, IC engine typical values describing the burning behavior in later combustion phases (i.e. burned mass fraction at 50% / 90%) should not be compared to measurements gathered with the *Flex-OeCoS*, which was optimized for optical investigation of ignition, combustion onset, and the early flame propagation process.

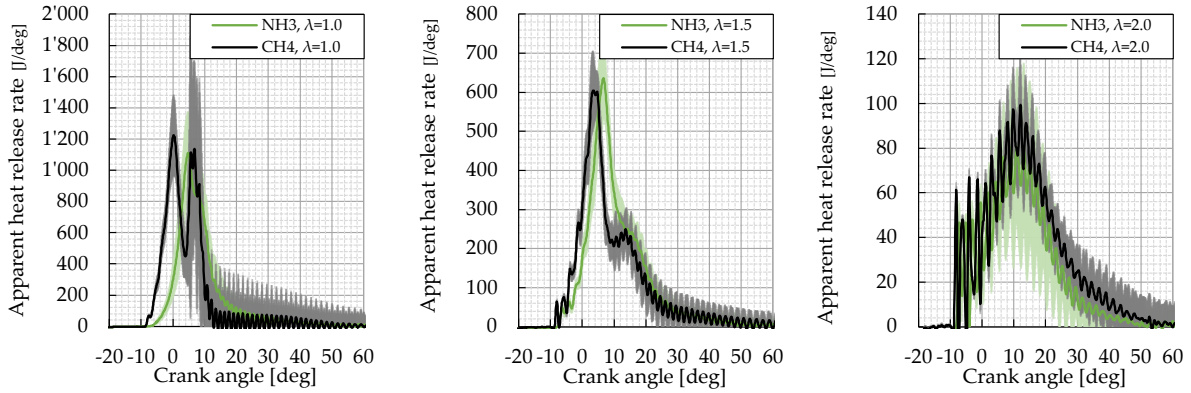

Figure 4: Apparent heat release rate (incl. standard deviation, pale color) of pilot fuel ignited ammonia vs. methane DF combustion for λ = 1.0 / 1.5 / 2.0 at operation parameters p_c = 70 bar, T_{in} = 50 °C, SOI = -10 °CA, ET = 500 µs.

The integrated burn rates shown in Figure 5 confirm the earlier starting and initially faster combustion for methane compared to ammonia. In the leanest case (λ = 2), the slow combustion speed of both ammonia and methane leave most of the fuel unconverted when the ongoing expansion stroke stops the combustion process. As mentioned before, the late combustion phase is strongly influenced by the staged combustion in the *Flex-OeCoS*, maximum fuel conversion rates cannot be compared to values observed in conventional engines with undivided combustion chambers. Further, the maximum conversion rates shown here are calculated from the apparent heat release rates and should be treated with caution since they cannot yet be validated by corresponding exhaust gas measurements. Despite the expected lower conversion rates compared to a conventional combustor, the *Flex-OeCoS* delivers a remarkably high conversion rate at λ = 1.5, which applies not only to methane but also to ammonia.

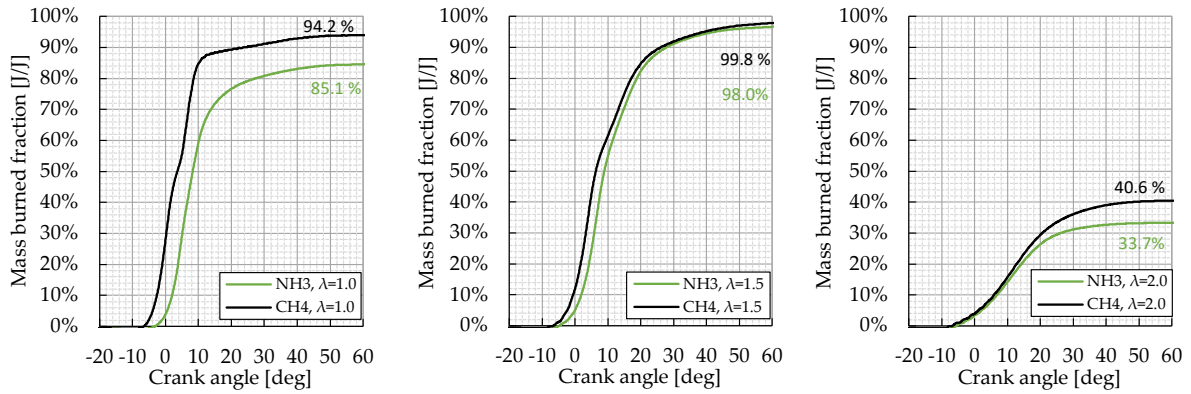

Figure 5: Integrated burn rate of pilot fuel ignited ammonia vs. methane DF combustion for λ = 1.0 / 1.5 / 2.0 at operation parameters p_c = 70 bar, T_{in} = 50 °C, SOI = -10 °CA, ET = 500 µs.

As described before, an apparent flame propagation speed s_{aFP} can be evaluated from the high-speed Schlieren measurements. The results in terms of λ-variation are shown in Figure 6 for both fuel cases. In the beginning it is difficult to differentiate the early flame evolution from the evaporating pilot spray. However, after the combustion propagates into the premixed charge, the calculated values are quite stable, especially when supported by the first detected OH*-radicals marking the start of combustion. As expected, the methane case exhibits a higher apparent flame propagation speed s_{aFP} in the early stage of (premixed) combustion compared to ammonia. In the following, an alignment towards an equivalent order of magnitude takes place. The changing volume due to the ongoing expansion stroke has an influence on the apparent flame propagation speed. Due to the fast start of combustion with high initial s_{aFP} this effect is weak in the compression stroke, but it can lead to an overestimation of low apparent flame propagation speeds in the expansion stroke. Nevertheless, it is an indication of the different flame propagation in terms of (local) transport phenomena in the early combustion phase. For higher air-fuel equivalence ratios, the slower combustion of leaner mixtures is not only reflected in the decreasing s_{aFP} but also in its slower decline back to zero.

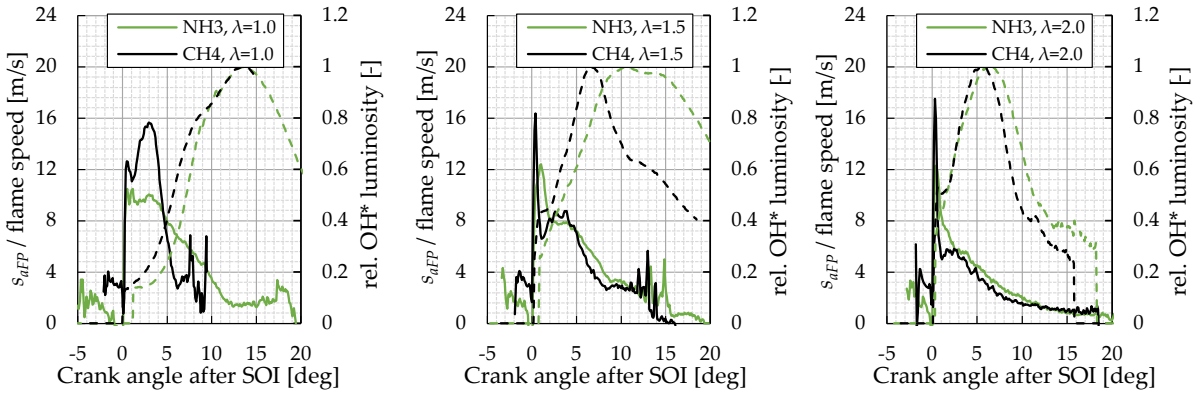

Figure 6: Apparent flame prop. speed (solid) and normalized luminosity (dashed) of OH radicals of pilot fuel ignited ammonia vs. methane DF combustion for λ = 1.0 / 1.5 / 2.0 at operation parameters p_c = 70 bar, T_{in} = 50 °C, SOI = -10 °CA, ET = 500 µs.*

A comparison between ammonia and methane dual-fuel combustion initiated by a dodecane pilot injection is shown in Figure 7 for a wider range of air-fuel equivalence ratios. It gives a more comprehensive insight into the cylinder pressures, apparent heat release rates, and burn rates. The apparent heat release rate in zoomed version shows the heat release of the pilot fuel which equals in terms of fuel amount 0.34% – 0.93% for ammonia (λ = 1.0 - 2.0) and 1.02% - 1.97% methane respectively. In terms of energy amount this means 0.81% - 2.22% for ammonia and 0.83% – 1.60% for methane.

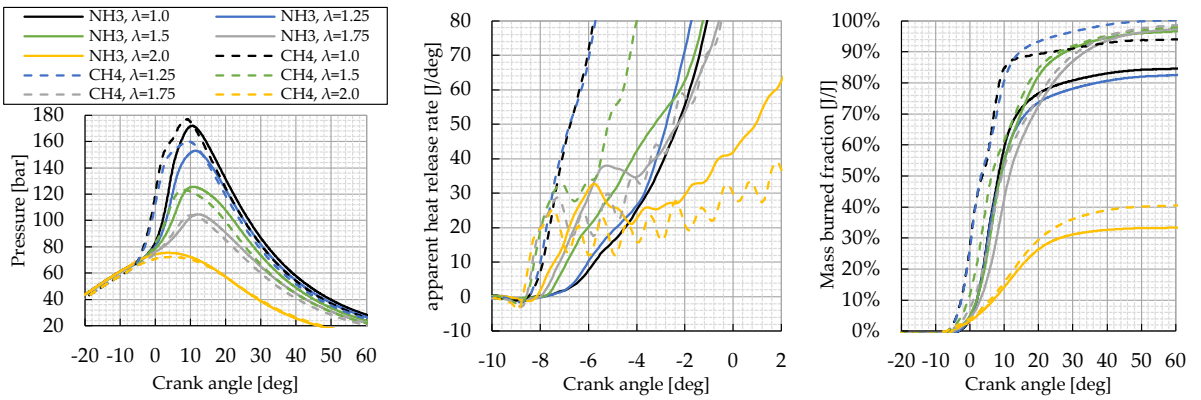

Figure 7: Cylinder pressure (left), zoomed aHRR (center) and integrated burn rate (right) of pilot fuel ignited ammonia vs. methane DF combustion for λ-variation between 1.0 and 2.0 at operation parameters p_c = 70 bar, T_{in} = 50 °C, SOI = -10 °CA, ET = 500 µs.

The ignition delay (*ID*) for different air-fuel equivalence ratios λ is difficult to discern exactly from the apparent heat release rate traces shown in Figure 4 respectively Figure 7. Thus, it is presented separately in Figure 8 for both, *ID* detection by way of the heat release rate calculation, and *ID* detection by analysis of the optical measurements. Time is defined from the effective (hydraulic) start of the pilot fuel injection (*SOI*). The *ID* values obtained from the *aHRR* calculation are in good agreement with the image analysis. As expected for dual-fuel combustion, ignition delay is increasing for lower air-fuel equivalence ratios λ, and maximal for stoichiometric conditions. However, for the ammonia case, the retarding influence on the ignition of the pilot fuel (*ID* gradient) is much more pronounced compared to methane dual-fuel combustion. This is due to the difference between the effective temperature in the cylinder at start of combustion and the temperature required for ignition which is quite smaller for methane according to its lower auto ignition temperature. Moreover, the high heat capacity of ammonia (which is almost three times higher than for air) results in lower end of compression temperatures T_c for higher fuel contents, which strongly influences the ignition delay.

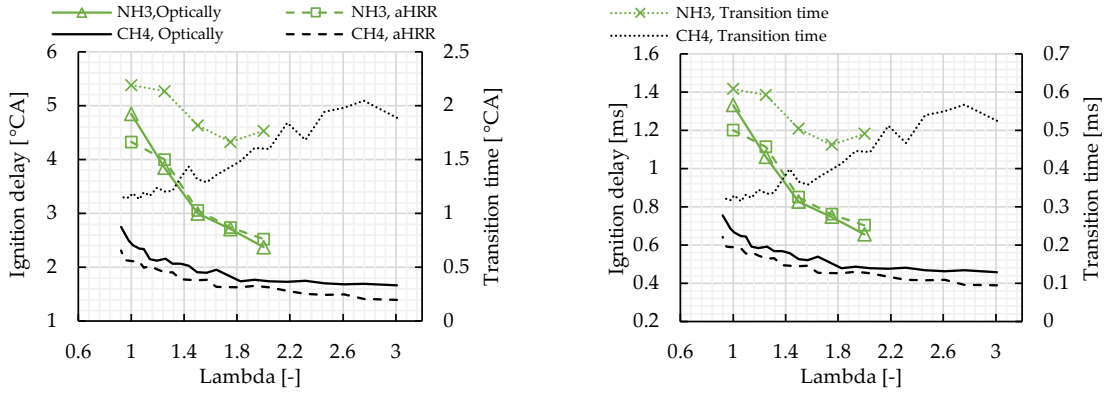

Figure 8: Ignition delay and transition time (CA resolved, left; time resolved, right) of pilot fuel ignited ammonia vs. methane DF combustion for λ-variation at operation parameters p_c = 70 bar, T_{in} = 50 °C, SOI = −10 °CA, ET = 500 µs.

The *transition time* shown in Figure 8 can be interpreted as the time required from ignition until the flame spreads out from the pilot fuel spray into the premixed charge. Longer ignition delays therefore lead to longer transition times because the spray volume is larger at the time of combustion. A reduced reactivity of the mixture due to lower temperature or fuel concentration also increases the transition times. For the methane case, the transition time increases monotonic towards higher air-fuel equivalence ratios – the reduced reactivity has a larger influence than the shorter ignition delay. For ammonia, however, the reduction of the ignition delay between λ = 1 and 1.5 overcompensates the reduction of the mixture reactivity which leads to decreasing transition times. Vice versa, an increased fuel content at lower λ increases the transition time due to lower in cylinder temperature affected by the higher heat capacity which decreases the reactivity as mentioned. It appears that the trend of higher transition time for lower λ is reversed at leaner mixtures λ > 1.75 when reactivity induced by the low fuel content prevails the lower in-cylinder temperature, and both fuels show comparable behavior.

In Figure 9 the crank angle position of the 50% mass burn fraction and the totally converted fuel mass is shown for the λ-variation. As mentioned before, those values can be used for comparisons between experiments in the *Flex-OeCoS*, but the staged combustion process prevents comparisons to corresponding values of commercial engines. As expected, the faster ignition respectively start of combustion for methane leads to earlier MBF50 positions compared to ammonia. The retarding effect of richer mixtures λ < 1.5 resulting in lowering the in-cylinder temperature, which shifts MBF50 towards later

crank angles. This is far more pronounced for ammonia but observable for methane as well, still recognizable in Figure 9 according to the flattening of the data trace towards lowest air-fuel equivalence ratios.

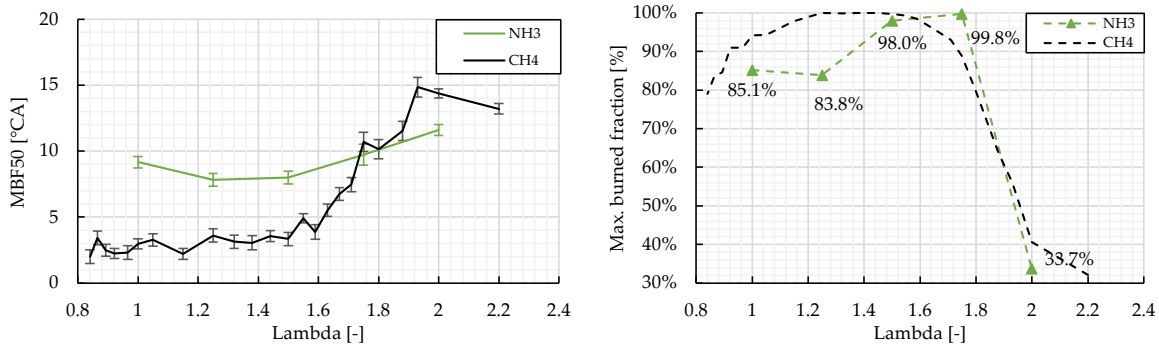

Figure 9: Mass burn fraction (MBF50, left) and max. burned fraction (right) of pilot fuel ignited ammonia vs. methane DF combustion for λ-variation at operation parameters p_c = 70 bar, T_{in} = 50 °C, SOI = −10 °CA, ET = 500 µs.

The total burned fraction given in Figure 9 (right) has been already described regarding burn rate in Figure 5 and gives an overview of the behavior in a wide range for both fuels. Whereas methane has an overall higher fuel conversion rate in a wide variation of different air-fuel equivalence ratios, the combustion of ammonia results in a high conversion ratio between λ = 1.5 and 1.75. This air-fuel region should be further investigated within following projects supported by exhaust gas measurements since a conversion ratio above 98% sounds very promising in terms of IC engine application.

Figure 10 shows the superimposed Schlieren/OH* chemiluminescence recordings of ammonia (top) and methane (bottom) combustion for the air-fuel equivalence ratio variation. The images are displayed in 1.0 °CA steps from -9 °CA to +2 °CA. Clearly observable is the long ignition delay for fuel-richer mixtures. In the stoichiometric case (λ = 1.0) of ammonia, the dodecane pilot spray is fully evaporated until -6.0 °CA, but the first flame kernel is only visible 1 °CA later. In the corresponding case for methane, ignition occurs long before the pilot spray is fully evaporated. The observable characteristic disappearance of the Schlieren signal at -6.0 °CA for ammonia is attributed to the first stage ignition respectively heat release of the low-temperature combustion that compensates the refractive index change due to mixture cooling from fuel evaporation. The long ignition delays for fuel-rich cases of ammonia shift the ignition spot and consecutively the center of combustion towards the bottom of the combustion chamber because the (evaporated) pilot fuel mixing with the premixed charge is still transported downwards from the momentum of the injection. Thus, combustion in the engine cylinder below starts early before the fuel in the combustion chamber is consumed. In the apparent heat release rates shown in Figure 4 this is observable in the far less pronounced "staged combustion" process of ammonia compared to methane. Additionally due to the lower combustion onset placement, the flame front travels a further distance simultaneous upward and downward within the combustion chamber. Therefore the lower relative flame speed overcomes due to synchronal combustion processes leading to a higher or equivalent heat release rate compared to methane at similar crank angle. For fuel-rich mixtures with λ = 1 and 1.25 at crank angle positions from 0 °CA onwards for ammonia resp. -3.0 °CA onwards for methane, transparent zones inside the combusted areas can be observed. These zones exhibit very low variations of the refractive index (which causes Schlieren signals), an indication of quite homogeneous, *hot zones* that span the whole combustion chamber width between the windows.

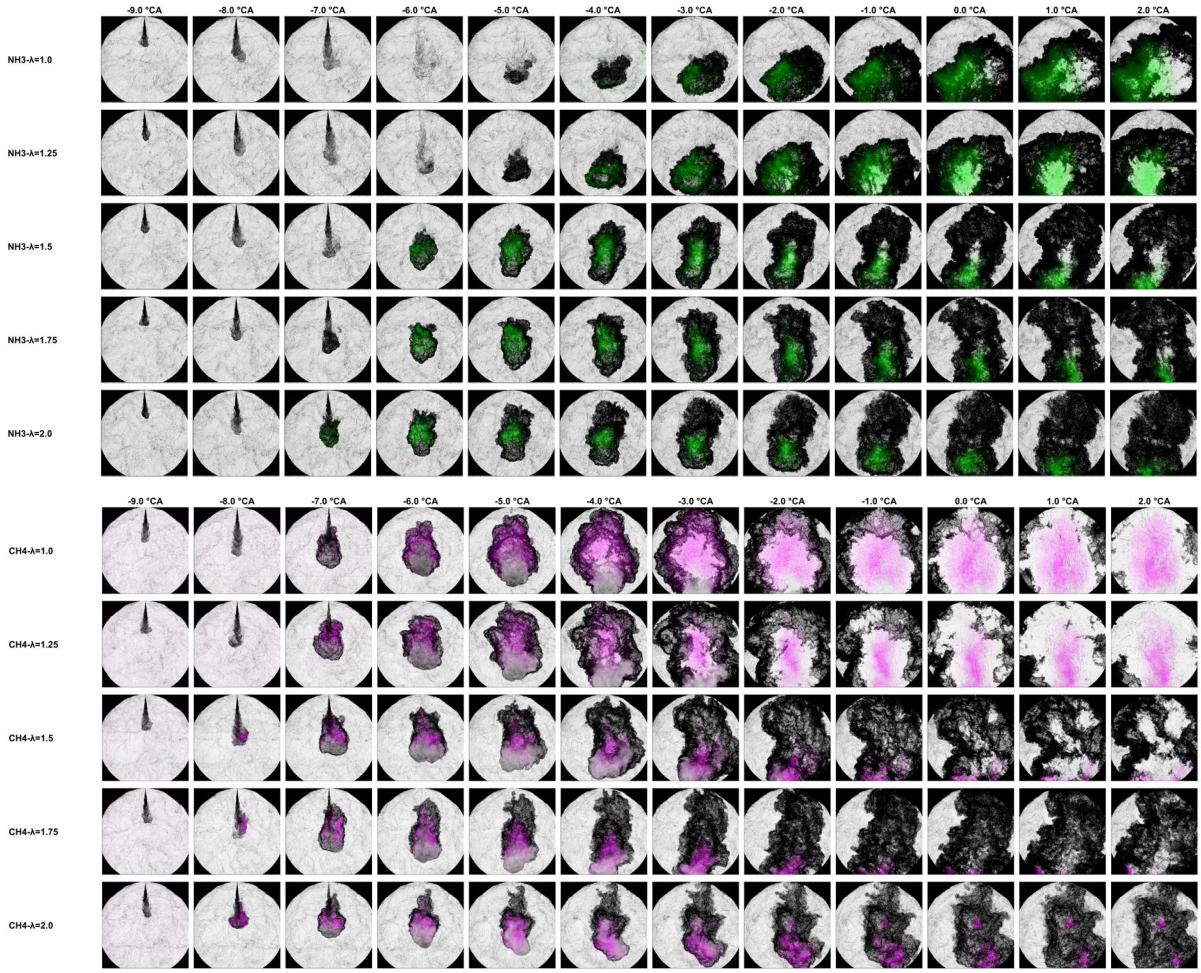

*Figure 10: Overlayed image sequences of simultaneously acquired high-speed Schlieren/OH*chemiluminescence recordings of pilot fuel ignited ammonia (top) and methane (bottom) DF combustion for different air-fuel equivalence ratios λ at operation parameters p_c = 70 bar, T_{in} = 50 °C, SOI = -10 °CA, and ET = 500 µs.*

3.2. Variation of start of pilot fuel injection (SOI)

A variation of pilot fuel injection for an air-fuel equivalence ratio of λ = 1.0 has been performed within a range of *SOI* = -20 °CA to +5 °CA. Thereby, the reference conditions such as compression pressure (p_c = 70 bar), intake temperature (T_{in} = 50°C), and pilot fuel injector actuation (*ET* = 500 µs) has been kept constant. The earliest and latest *SOI* were not suitable depending on the fuel case: For methane, the *SOI* = -20 °CA case was not applicable due to hard knocking phenomena; for ammonia, very late timing of *SOI* = +5 °CA with corresponding temperatures, led to misfire and high ammonia slip – thus, followed by an abort of the experiment. Depending on the timing of injection, the pilot fuel is supplied into the premixed ammonia/air charge at different pressure and temperature levels. The corresponding in-cylinder temperature levels for different *SOI* have already been investigated in detail and determined [14]. Accordingly, for *SOI* = -20 °CA the pilot fuel is injected into the mixture under pressure respectively temperature states of about $p \approx 42$ bar and $T \approx 725$ K. At piston top dead center (*TDC*) the conditions for the mixture reveal approximately of $p \approx 70$ bar and $T \approx 820$ K. The reference case of *SOI* = -10°CA exposes pressure/temperature conditions of about p = 60 bar and $T \approx 790$ K. Moreover, especially for very early pilot fuel injections, the ongoing compression stroke will considerably increase pressure as well as temperature levels during the fuel mixing process, respectively between *SOI* and ignition.

Figure 11 shows the resulting pressure traces for the different *SOI* at given air-fuel equivalence ratios for both fuels, ammonia as well as methane. If we first look at *SOI* variation for the methane case (right), the ignition timing shift is easily recognizable resulting in a later pressure evolution. The earliest injection at *SOI* = -20 °CA has not been performed for methane for λ = 1.0 due to safety reasons since the combustion initiated at *SOI* = -15 °CA already revealed a knocking combustion behavior when reaching the squish gap within the cylinder bore (around -1 °CA). The entire combustion has taken place at nearly a constant rising CA delay, which implicates a mostly linear behavior of the ignition delay. On the other hand, for the ammonia case the results are not that distinct, and therefore must be discussed in detail. Firstly, for latest pilot fuel injection *SOI* = +5 °CA no combustion has taken place, and therefore the experiment had to be stopped in view of ammonia slip. On the other hand, a very early pilot fuel injection (*SOI* = -20 °CA) could have been performed since ammonia did not exhibit any knocking behavior at those operation conditions. Thus, focusing *SOI* = -10 / -5 / 0 °CA a similar pattern to methane is recognizable, and the combustion acts directly to the later pilot fuel injection. Looking at the pressure development at *SOI* = -15 °CA, it is noticeable that the pressure curve does not rise by the same time amount earlier. Therefore, it can be assumed that the ignition delay or the transition time is longer at this specific in-cylinder temperature. The overlaid standard deviation for the pressure curve is already slightly larger than for the other operating points, which is due to a higher coefficient of variation (COV) for the combustion. Looking at the earliest pilot fuel injection at *SOI* = -20°C, a much later average pressure increase is observable than for the case *SOI* = -15°CA. Considering the standard deviation (hatched grey area), apparently everything between misfire and combustion compared to pilot fuel injection at *SOI* = -15 °CA is present. This behavior will be further discussed in a following section by means of the optical measurement results.

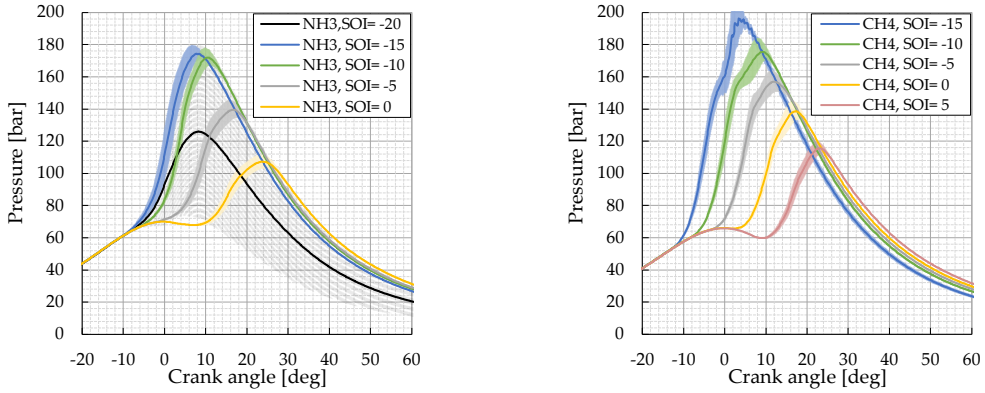

Figure 11: Cylinder pressure of pilot fuel ignited ammonia (left) vs. methane (right) DF combustion for the given SOI-variation (-20 to 0 resp. -15 to 5) at operation parameters λ = 1.0, p_c = 70 bar, T_{in} = 50 °C, ET = 500 µs.

The apparent heat release rate shown in Figure 12 is represented in a shifted (relative) crank angle format whereas 0 °CA always marks the event of the start of injection (*SOI*). Thus, the resulting heat release gradients and its relative position can be compared directly for every operation process point.

For the ammonia case (left), the first *aHRR* rise (up to around 40 J/deg) denotes the combustion of the dodecane pilot fuel. In the following, a slowly steady increase of the *aHRR* of the main charge takes place in general. However, for the early start of injection (*SOI* = -15 °CA) as well as for *TDC* (*SOI* = 0 °CA) the *aHRR* gradient is not as steep than for the other cases (*SOI* = -5 /-10 °CA) due to reduced reactivity. On the one hand, the *SOI* = -15 °CA case exhibits a longer ignition delay due to lower in-cylinder temperature but afterwards, around 14 °CA after *SOI* the *aHRR* increases with a comparable gradient to a similar level than the *SOI* = -10 °CA case. The late pilot fuel injection case

SOI = 0 °CA does not suffer from a high pilot fuel ignition delay, since the in-cylinder temperature is nearly at maximum at *TDC*, and therefore shows an early initial rise of the *aHRR* marking the ignition of the pilot fuel. On the other hand, the *aHRR* for the main charge exhibits a significantly lower gradient, which can be explained by two aspects: Firstly, the temperature already drops after *TDC*; secondly (even more pronounced), the rapid decrease of turbulence within the cylinder decreases the turbulent flame speed, and hence reducing the reaction rate resulting in an even lower *aHRR* for late *SOI*.

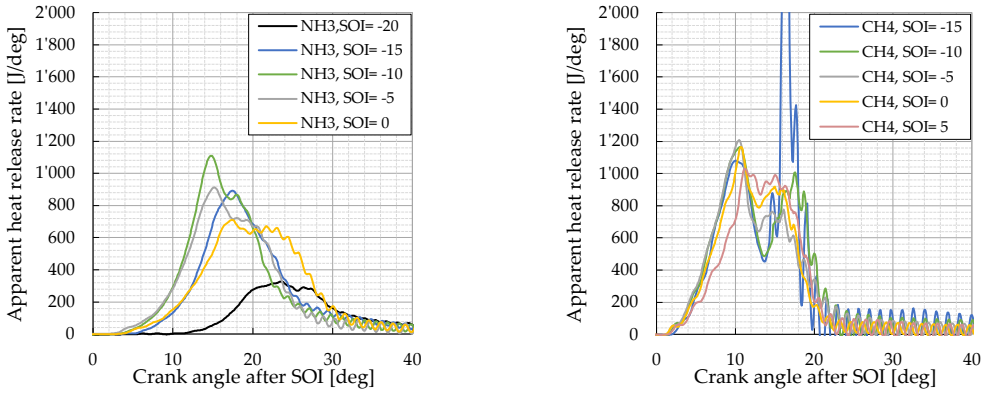

Figure 12: Apparent heat release rate of pilot fuel ignited ammonia (left) vs. methane (right) DF combustion for the given SOI-variation (-20 to 0 resp. -15 to 5) at operation parameters λ = 1.0, p_c = 70 bar, T_{in} = 50 °C, ET = 500 µs.

For the methane case, this effect can be recognized as well looking at Figure 12 (right) when comparing *SOI* = -5 °CA and *SOI* = 5 °CA. Neglecting wall heat transfer, the in-cylinder temperature for both cases is nearly the same by process definition, so that early *aHRR* can behave in similar manner, while the decreasing turbulence is reducing the reaction rate. Furthermore, the decompression effect after *TDC* does lead to a lowering of the combustion temperature compared to *SOI* = -5°CA, but this effect is rather prominent for later times after *SOI* due to the little piston movement around *TDC*. For the earliest start of pilot injection *SOI* = -15°CA, the apparent knocking, which occurred in the squish gap area, is very well recognizable at around 16 °CA according to the tremendous heat release level and the subsequent oscillation caused by the rapid increase in heat release.

The integrated apparent heat release rate nominated by the total fuel energy content, which is called the integrated burn rate, is displayed in Figure 13. This specific analysis greatly reveals the fuel conversion rate in terms of start of pilot fuel injection (*SOI*) and its characteristics for both fuel cases, ammonia, and methane.

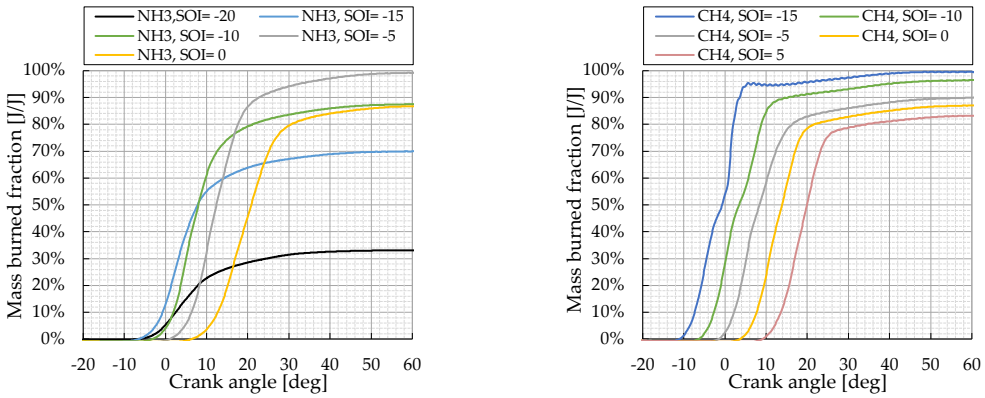

Figure 13: Integrated burn rate of pilot fuel ignited ammonia (left) vs. methane (right) DF combustion for the given SOI-variation (-20 to 0 resp. -15 to 5) at operation parameters λ = 1.0, p_c = 70 bar, T_{in} = 50 °C, ET = 500 µs.

Thereby the methane case exhibits the expected course of the fuel conversion rate very well. The distinctive staged combustion recognizable in Figure 12, and discussed earlier within the air-fuel equivalence ratio variation, is represented very well, and vanishes away for later starts of pilot fuel injection (*SOI*). Due to expansion, which leads to an increasing squish height and thus reduced turbulence, the *aHRR* is lower when the combustion reaches the squish gap area. Later *SOI* are leading to a lower total fuel conversion rate and thereby a high level of methane slip. For Ammonia, the fuel conversion rate at given engine speed does not have this monotonic trend. Moreover, the fuel conversion rate follows the already described influences which are leading to a lower pressure evolution or lower *aHRR*, and thus to a lower efficiency.

The apparent flame propagation speed s_{aFP} is shown in Figure 14, again crank angle shifted displayed in terms of the start of combustion (*SOC*). It shows the general trend for *SOI* variation compared to the air-fuel equivalence ratio variation presented before. During the first combustion phase s_{aFP} for ammonia is yielding around 10 m/s as expected for λ = 1, and around 14 – 16 m/s for methane. Even though the apparent flame propagation speed is affected by the expansion stroke, the s_{aFP} decrease of methane observed from three degrees after *SOI* is quite similar in terms of its decline. The low reactivity of ammonia at *SOI* = -20 °CA is confirmed by the optical measurement analysis, which yield in an initially low s_{aFP}, and with only 8 m/s very late in the process never reaching the full propagation speed compared to other cases. This low s_{aFP} leads to a low conversion rate, and hence to the low integrated burn rate.

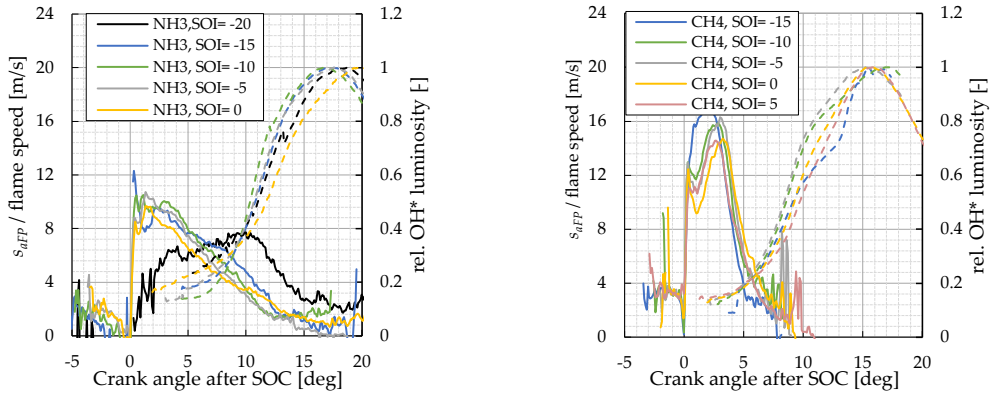

Figure 14: Apparent flame propagation speed (solid) and normalized luminosity (dashed) of OH radicals of pilot fuel ignited ammonia (left) vs. methane (right) DF combustion for given SOI-variation (-20 to 0 resp. -15 to 5) at operation parameters λ = 1.0, p_c = 70 bar, T_{in} = 50 °C, ET = 500 µs.*

As shown in Figure 15, the ignition delay values obtained from the *aHRR* calculation are again (as for the air-fuel equivalence ratio variation) in good agreement with those of the optical measurement analysis – except for the methane *SOI* = 5 °CA case, where a misinterpretation of the *aHRR* based *ID* of around 0.7 ms compared to the "optical" ignition delay with 2.0 ms occurred. Ammonia is more prune for ignition delay retardation due to relatively colder charge conditions for early *SOI* than it is for methane. Transition time for methane thereby remains nearly constant over the entire *SOI*-variation or even shows an opposite trend against ammonia. It is probably due to the differentiation between ignition delay and transition time, whereas the *ID* related time was slowly overestimated, and the transition time therefore underestimated. This could probably happen due to the threshold value set for the integrated *aHRR* slightly above the energy content of the pilot fuel. The transition time for ammonia at early *SOI* = -20 °CA is thereby very high with 11.5 °CA respectively 3.2 ms and represents the already known behavior of a combustion that is ignited below its minimum required temperature for flame propagation.

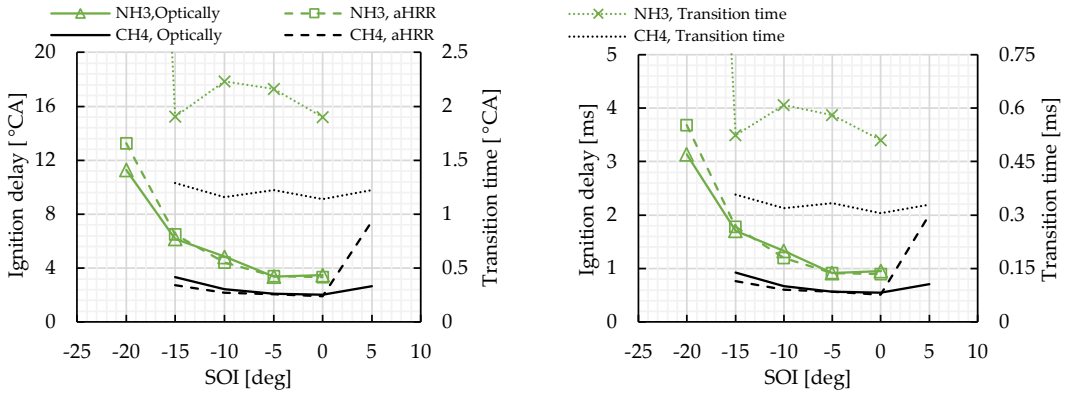

Figure 15: Ignition delay and transition time (CA resolved, left; time resolved, right) of pilot fuel ignited ammonia vs. methane DF combustion for given SOI-variation (-20 to 0 resp. -15 to 5) at operation parameters $\lambda = 1.0$, $p_c = 70$ bar, $T_{in} = 50$ °C, ET = 500 µs.

The longer *ID* for ammonia can now be compensated in terms of an earlier *SOI* to achieve the same start of combustion (*SOC*). Thereby, ignition delay and transition time for the ammonia case can be summed and added with the difference to the related *SOI* for methane case to get a nearly same start of combustion – i.e. for a desired *SOI* at -10 °CA (methane case) the ammonia must be ignited at least 3.3 °CA earlier to achieve the same *SOC*. This may be an acceptable correction if the burn rates for both fuels remain nearly the same. Since the time required to achieve the full charge is important to get the correct pressure evolution, it is possible to compare the MBF50 in terms of both used fuels, as shown in Figure 16. For the *SOI* = -10 °CA case a difference of 4 °CA is recognizable, which implicates that the burn rate is slightly lower at given operation conditions. This is the amount the *SOI* should be set earlier to achieve similar combustion when using ammonia instead of methane. The overall fuel conversion rate given as maximum burned fraction displayed in Figure 16 (right) must be considered as well. The fuel conversion rate is dropping significantly for ammonia when not employing the optimal start of pilot injection at *SOI* = -5 °CA. Hence, the in-cylinder temperature is too low compared to the one at *TDC* when combusting the main charge. Therefore, an earlier *SOI* should be possible applying an elevation of the compression temperature by increasing the compression ratio.

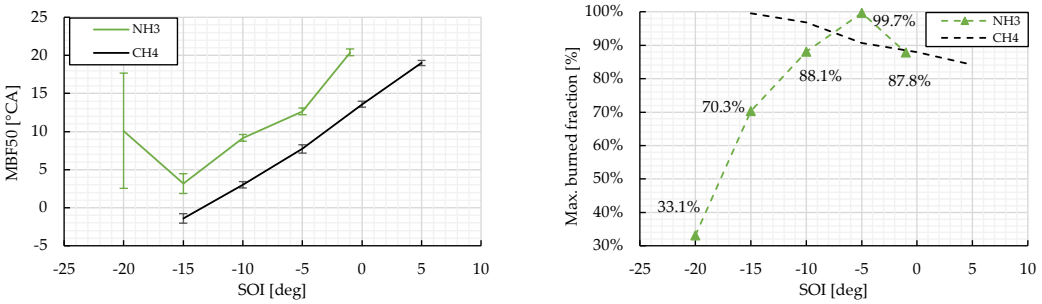

Figure 16: Mass burn fraction (MBF 50%, left) and max. burned fraction (right) of pilot fuel ignited ammonia vs. methane DF combustion for given SOI-variation (-20 to 0 resp. -15 to 5) at operation parameters $\lambda = 1.0$, $p_c = 70$ bar, $T_{in} = 50$ °C, ET = 500 µs.

Figure 17 shows the superimposed Schlieren/OH* chemiluminescence recordings of ammonia (top) and methane (bottom) combustion for corresponding *SOI*-variation. The images are displayed in a relative time axis in steps of 1.0 °CA from 0.3 °CA to 11.3 °CA. For the ammonia case, it must be noted that the earliest start of pilot injection at *SOI* = -20 °CA comprises the widest averaging since the *COV* (discussed earlier) results from a broad band rising from nearly misfire to very rapid combustion. The ignition delay identifiable from the image sequence of the particular cycle shown in Figure 17 is the closest but still lower than the average *ID* value. The optical interpretable ignition delay variation for

ammonia is much higher than for methane, where it generally lies within 1.0 °CA. Pilot fuel ignition is noticeable later for ammonia, whereas the evaporation of the pilot fuel is fully completed for early *SOI* = -15/-20 °CA before combustion onset is visible. Since the identical pilot fuel has been applied for both fuels, the interaction between dodecane and main charge must be the key driver. Due to the higher heat capacity of ammonia, the charge leads to lower in-cylinder temperatures during compression causing a longer ignition delay. Moreover, due to the high activation energy of ammonia necessary for dissociation and combustion onset, less energy is available for the pilot fuel auto-ignition. However, these complex processes of pilot fuel evaporation, charge entrainment and mixing, combined with chemical reactions should be further investigated by means of advanced optical diagnostics.

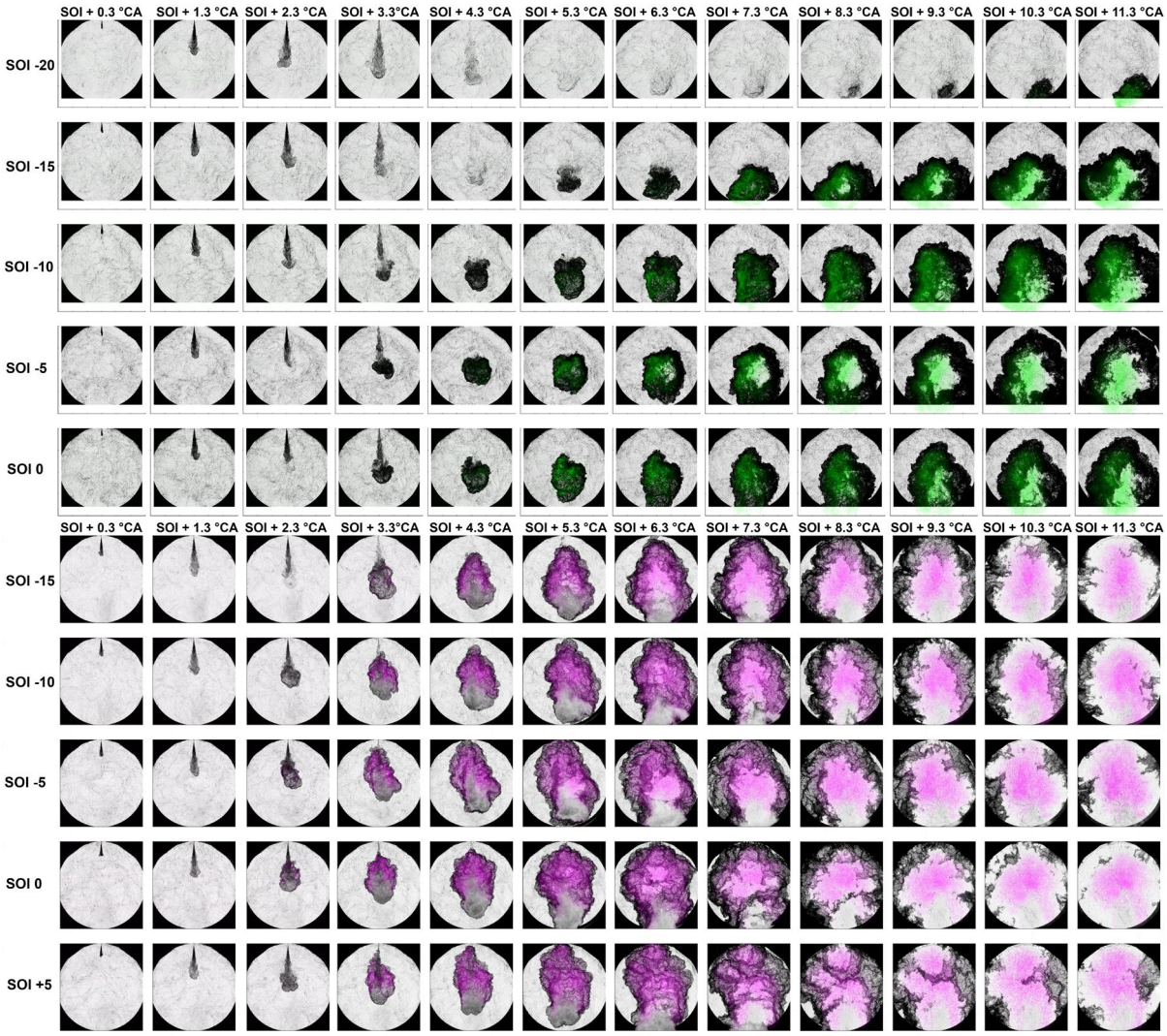

*Figure 17: Overlayed image sequences of simultaneously acquired high-speed Schlieren/OH*chemiluminescence recordings of pilot fuel ignited ammonia (top) and methane (bottom) DF combustion for different SOI at operation parameters $\lambda = 1$, $p_c = 70$ bar, $T_{in} = 50$ °C, SOI = -10 °CA, and ET = 500 µs.*

The *hot zones* discussed for the air-fuel equivalence ratio variation easily recognizable for the methane cases and covering the main area during later combustion phases, are less pronounced for the ammonia combustion but a high area share of the *hot zones* is representing a hot combustion and therefore a high conversion rate. The "white-grey" areas in the pilot fuel of the methane image sequences are an indication of soot formation at the spray tip due to interference of OH* chemiluminescence with soot incandescence. Its absence in the ammonia case during pilot fuel combustion underlines the deficiency of soot production.

4. Conclusions

Premixed ammonia dual-fuel combustion initiated by a dodecane pilot fuel could be successfully executed at the optically accessible test facility *Flex-OeCoS*. A variation of air-fuel equivalence ratio λ as well as start of injection (*SOI*) has been performed. The characteristics of the ammonia combustion process is compared to analogous methane dual-fuel combustion with same operation conditions. The well-known boundary conditions allow a precise acquisition of pressure and temperature to enable thermodynamic analysis in view of ignition delay, dual-fuel transition time, heat release, and IC engine related results such as mass burned fraction. Moreover, the optical accessibility of the *Flex-OeCoS* allows simultaneous Schlieren/OH* chemiluminescence high-speed recordings of the corresponding combustion processes, based on which an optically analyzed ignition delay as well as an apparent flame propagation speed could be determined. In addition, qualitative statements can also be made regarding spatial start of combustion or formation of soot within the combustion chamber.

The variation of air-fuel equivalence ratio variation between λ = 1.0 and λ = 2.0 delivers deeper insight in λ-dependent mass burned fuel amount, which is ideal in the range of λ = 1.5 and λ = 1.8 for given test facility operation conditions. The ammonia slip is expected to be low since the fuel conversion rate is high between 98.0% and 99.8% based on *aHRR* calculations. However, since exhaust gas measurements are (currently) not yet possible (but planned), this result cannot yet be confirmed independently. Ignition delay determined for ammonia is generally higher, e.g. 0.82 ms compared to 0.49 ms for methane at λ = 1.5 and should be considered in terms of fuel application in an IC engine. The transition time, based on the pilot fuel auto-ignition and premixed charge combustion onset, is more influenced by the higher heat capacity of ammonia at given operation conditions. Thus, for a lower air-fuel equivalence ratio it is longer, e.g. 0.5 ms compared to 0.35 ms for methane at λ = 1.5. The small amount of pilot fuel quantity (versus total energy content) of 0.81% – 2.22% for ammonia and 0.83% – 1.60% for methane, respectively, appears to be sufficient in the range of λ = 1.0 to λ = 2.0 to provide a reliable ignition source regarding the particular combustion chamber design of the *Flex-OeCoS* test facility.

The apparent turbulent flame propagation speed s_{aFP} determined from the optical high-speed recordings (at average turbulence intensity *u'* of 3.6 m/s before *TDC*) can be given for λ = 1.0 during the early flame propagation phase with about 10 m/s compared to methane with around 14 m/s. For λ = 1.5 the s_{aFP} examined is around 8 m/s for both fuels and represent therefore a similar rate of heat release.

The variation of start of injection (*SOI*) provides corresponding information on ignition delay, transition time and combustion behavior of both, pilot and main combustion, via the direct coupling to in-cylinder gas temperature. A very early start of injection (at low temperatures) of the pilot fuel thereby leads to an adverse combustion, hence fuel has already spread out before ignition onset and thus energy density within the pilot combustion already lowered. Moreover, slow combustion transition and possibly incomplete combustion can lead to high ammonia slip. On the other hand, a controlled long(er) *ID* can lead to a spatial deeper placement of the combustion onset within the combustion chamber, which leads to a larger flame surface, and hence a higher global heat release rate.

The optical high-speed Schlieren/OH* chemiluminescence recordings do support classic measurements optimally and give spatially resolved deeper insight into ignition and combustion behavior. In addition, it can be qualitatively stated that the local soot production at the dodecane pilot fuel spray could not be recognized within ammonia combustion compared to methane.

Based on these promising results further investigations are planned. Especially exhaust gas measurement is an important next step, which should give insight into ammonia slip as well as NO_X production. Furthermore, those investigations should yield validation data for calculated fuel conversion ratios. A wider range and finer resolved air-fuel equivalence ratio variation at elevated compression temperatures will be a next step to evaluate the optimal combustion process using ammonia as fuel. An additional important future investigation is the variation in pilot-fuel amount using parameters such as duration of injection, nozzle diameter as well as rail pressure, in view of combustion stability.

Literature

[1] United Nations, "Paris Agreement", 2015, http://unfccc.int/files/essential_background/convention/application/pdf/english_paris_agreement.pdf.

[2] DNV Energy Transition Outlook 2020 (Det Norske Veritas), "*Maritime Forecast to 2050*".

[3] F. Abbasov, T. Earl; C. Calvo Ambel, B. Hemmings, L. Gilliam, "*Roadmap to decarbonising European shipping*". T&E - Transport & Environment, 2018.

[4] N. Ash, T. Scarbrough, "*Sailing on Solar – Could green ammonia decarbonise international shipping?*". Environmental Defense Fund, 2019.

[5] Lloyd's Register, UMAS (2019a), "*Fuel production cost estimates and assumptions*", Lloyd's Register; UMAS, 2019.

[6] Lloyd's Register, UMAS (2019b), "*Zero-Emission Vessels: Transition pathways*". Low Carbon Pathways 2050 series, Lloyd's Register; UMAS, 2019.

[7] Lloyd's Register; UMAS (2020), "*Techno-economic assessment of zero-carbon fuels*". Lloyd's Register; UMAS, 2020.

[8] P. Osterkamp, T. Smith, K. Søgaard, "*Five percent zero emission fuels by 2030 needed for Paris-aligned shipping decarbonization*", Global Maritime Forum. Getting to Zero Coalition (ed.), 2021.

[9] B. Schneider, C. Schürch, K. Boulouchos, S. Herzig, M. Hangartner, D. Humair, S. Wüthrich, C. Gossweiler, K. Herrmann, "*The Flex-OeCoS – a Novel Optically Accessible Test Rig for the Investigation of Advanced Combustion Processes under Engine-Like Conditions*", Energies 2020, 13(7), 1794; https://doi.org/10.3390/en13071794.

[10] S. Wüthrich, D. Humair, K. Herrmann, A. Bertola, "*Enhanced instrumentation of an optical research engine with unique combustion chamber*", 14th Int. AVL Symposium on Propulsion Diagnostics, June 23-24, 2020, Baden-Baden, Germany. ISBN 978-3-9816971-6-2.

[11] D. Humair, P. Cartier, P. Süess, S. Wüthrich, K. Herrmann, C. Barro, B. Schneider, C. Schürch, K. Boulouchos, "*Characterization of dual-fuel combustion processes*", Rostock 6th Large Engine Symposium, September 3-4, 2020, ISBN 978-3-941554-22-1.

[12] W. Vera-Tudela, B. Schneider, S. Wüthrich, K. Herrmann, "*Study on the ignitability of a high-pressure direct-injected methane jet using a diesel pilot, a glow-plug and a prechamber*", IJER-21-0139, 2021, https://doi.org/10.1177/14680874211048144.

[13] W. Vera-Tudela, B. Schneider, S. Wüthrich, K. Herrmann, "*Study on the ignitability of a high-pressure direct-injected methane jet using a scavenged pre-chamber under a wide range of conditions*", IJER-1-14, 2022, https://doi.org/10.1177/14680874221093144.

[14] S. Wüthrich, P. Cartier, P. Süess, B. Schneider, P. Obrecht, and K. Herrmann, "*Optical investigation and thermodynamic analysis of premixed ammonia dual-fuel combustion initiated by dodecane pilot fuel*", Fuel Communications 12 (2022) 100074, https://doi.org/10.1016/j.jfueco.2022.100074.

[15] J.M. Desantes, J.M. García-Oliver, W. Vera-Tudela, D. López-Pintor, B. Schneider, K. Boulouchos, "*Study of the auto-ignition phenomenon of PRFs under HCCI conditions in a RCEM by means of spectroscopy*", Applied Energy, Vol. 179, pp. 389-400, 2016, https://doi.org/10.1016/j.apenergy.2016.06.134.

[16] A. Srna, M. Bolla, Y.W. Wright, K. Herrmann, R. Bombach, S.S. Pandurangi, K. Boulouchos, G. Bruneaux, "*Ignition characteristics of n-dodecane pilot fuel spray in a premixed compressed methane/air charge*". Proceedings of the Combustion Institute 37 (2019) 4741–4749. https://doi.org/10.1016/j.proci.2018.06.177.

[17] J.M. Desantes, J.V. Pastor, J.M. García-Oliver, W. Vera-Tudela, "*An experimental study of the effects of fuel properties on reactive spray evolution using Primary Reference Fuels*", Fuel, Vol. 163, pp. 260-270, 2016, https://doi.org/10.1016/j.fuel.2015.09.064.

[18] A. Srna, R. Bombach, K. Herrmann, G. Bruneaux, "*Characterization of the spectral signature of dual-fuel combustion luminosity: implications for evaluation of natural luminosity imaging*", Applied Physics B (2019) 125:120, https://doi.org/10.1007/s00340-019-7222-z.

[19] P. Obrecht, "*WEG: calculation of the heat development law based on measured combustion chamber pressure traces*", in-house thermodynamic model, ETHZ-LAV & FHWN-ITFE, 2021.

[20] S. Wüthrich, D. Humair, K. Herrmann, A. Bertola, "*Enhanced instrumentation of an optical research engine with unique combustion chamber*", 14th Int. AVL Symposium on Propulsion Diagnostics, June 23-24, 2020, Baden-Baden, Germany. ISBN 978-3-9816971-6-2.

[21] J. Schramm, J. N. Klüssmann, L. R. Ekknud, A. Ivarsson, "*Ammonia Application in IC Engines*", 2020.

[22] C. Mounaïm-Rousselle, P. Bréquigny, C. Dumand, and S. Houillé, "*Operating Limits for Ammonia Fuel Spark-Ignition Engine*", Energies (14), 2021, https://doi.org/10.3390/en14144141.

[23] C. Lhuillier, P. Brequigny, F. Contino, and C. Mounaïm-Rousselle, "*Experimental study on ammonia/hydrogen/air combustion in spark ignition engine conditions*", Fuel (269), 2020, https://doi.org/10.1016/j.fuel.2020.117448.

[24] S. McAllister, J.-Y. Chen, and A. C. Fernandez-Pello, "*Fundamentals of Combustion Processes: Appendix*", New York, NY: Springer New York, 2011.

[25] S. Frankl, S. Gleis, S. Karmann, M. Prager, and G. Wachtmeister, "*Investigation of ammonia and hydrogen as CO2-free fuels for heavy duty engines using a high-pressure dual-fuel combustion process*", IJER, vol. 22, no. 10, pp. 3196–3208, Oct. 2021, https://doi.org/10.1177/14680874209678 73.

[26] D. Han, Y. Liu, and Z. Huang, "*The Use of Ammonia as a Fuel for Combustion Engines*", Engines and Fuels for Future Transport, G. Kalghatgi, A. K. Agarwal, F. Leach, and K. Senecal, Eds. Singapore: Springer Singapore, 2022, pp. 233–256.